Scientific Research Publishing

Applied Mathematics, 2025, 16(11), 752-784
https://www.scirp.org/journal/am
ISSN Online: 2152-7393
ISSN Print: 2152-7385

Numerical Investigation of Magnetohydrodynamic (MHD) Natural Convection in a Nanofluid Filled Trapezoidal Cavity Considering the Use of Obstacle Shape, Wall Corrugation, and Inclination Angle

Sree Pradip Kumer Sarker*, Md. Mahmud Alam

Department of Mathematics, Dhaka University of Engineering and Technology (DUET), Gazipur, Bangladesh
Email: *pradip.duet@gmail.com, alamdr.mahmud@duet.ac.bd

How to cite this paper: Sarker, S.P.K. and Alam, Md.M. (2025) Numerical Investigation of Magnetohydrodynamic (MHD) Natural Convection in a Nanofluid Filled Trapezoidal Cavity Considering the Use of Obstacle Shape, Wall Corrugation, and Inclination Angle. *Applied Mathematics*, **16**, 752-784.
https://doi.org/10.4236/am.2025.1611040

Received: October 19, 2025
Accepted: November 8, 2025
Published: November 11, 2025

Copyright © 2025 by author(s) and Scientific Research Publishing Inc.
This work is licensed under the Creative Commons Attribution International License (CC BY 4.0).
http://creativecommons.org/licenses/by/4.0/

Open Access

Abstract

This study presents a numerical investigation of magnetohydrodynamic (MHD) natural convection in a nanofluid-filled trapezoidal cavity, focusing on the combined effects of internal obstacle shape, wall corrugation, and inclination angle. Using Cu-H_2O nanofluid and the finite element method, simulations were performed for Rayleigh numbers ranging from 10^3 to 10^6, Hartmann numbers from 0 to 50, and inclination angles of 15˚, 30˚, and 45˚. Results show that both obstacle geometry and wall corrugation profile strongly influence thermal performance. Square-shaped obstacles with triangular wavy walls achieved the highest Nusselt numbers, while sinusoidal walls provided superior thermodynamic efficiency, particularly at lower inclination angles. Increasing Hartmann numbers suppressed convective motion, as reflected by decreased Nu and ECOP values across all cases. The influence of geometric features, specifically obstacle shape and wall corrugation, was found to be most significant at low Rayleigh numbers, where buoyancy-driven flow is weaker and geometric modulation governs heat transport. The optimal configuration for enhanced heat transfer and energy efficiency was identified as square obstacles with sinusoidal or triangular walls at a 15˚ inclination and low Ha. These findings offer valuable guidance for designing thermally efficient enclosures in electronics cooling, solar collectors, and microfluidic systems, where controlling convection under magnetic effects is essential.

Keywords

MHD Natural Convection, Nanofluid Heat Transfer,
Trapezoidal Enclosure, Wall Corrugation,
Entropy Generation

1. Introduction

Natural convection in enclosures is a fundamental mechanism widely utilized in thermal management systems such as electronic cooling devices, solar energy collectors, and energy-efficient building designs [1]. The performance of these systems has seen considerable improvement through the introduction of nanofluids, fluids containing suspended nanoparticles that enhance thermal conductivity and heat transport characteristics [2]. Due to their superior thermophysical properties, nanofluids have been effective in optimizing convective flow behavior across various boundary and geometric configurations [3].

The integration of internal heat-generating obstacles within cavities has a pronounced impact on natural convection patterns. These effects are closely tied to the obstacle's shape, size, and thermal loading [4]. Common geometries such as circular, square, elliptical, and triangular obstacles have demonstrated their ability to influence local flow recirculation, vortex formation, and overall heat transfer performance [5]. Additionally, the inclination of the cavity introduces a gravitational asymmetry that modifies buoyancy-driven forces, further affecting flow circulation and entropy generation [6].

When magnetic fields are applied, magnetohydrodynamic (MHD) effects arise, characterized by the Hartmann number. These effects tend to suppress convective motion due to the Lorentz force, thereby altering the dominant heat transfer mode from convection to conduction [7]. Nonetheless, careful tuning of magnetic field intensity can lead to improved temperature control and thermal uniformity in nanofluid-filled enclosures [8]. The shape and placement of internal obstacles, such as square or triangular blocks, have been shown to enhance boundary layer disturbance, leading to better convective performance [9] [10]. Inclined cavities filled with nanofluids are of particular interest as changes in inclination affect the alignment between thermal gradients and gravity, thus influencing heat transfer effectiveness and entropy generation [11] [12]. These effects become more complex in the presence of magnetic fields, where interactions between geometric design, thermal forces, and electromagnetic suppression must be considered simultaneously [13].

In recent studies, cavity wall modifications, especially wavy or corrugated surfaces, have demonstrated the ability to create secondary vortices, thereby improving heat transfer rates and flow mixing [14] [15]. At the same time, the use of hybrid nanofluids, composed of multiple types of nanoparticles, offers enhanced control over thermophysical properties like conductivity and viscosity [16]. Com-

posite cavities with porous structures or layered domains further enhance energy transport efficiency by introducing porosity and permeability effects [17] [18]. Performance optimization has also been linked to nanoparticle shape, volume fraction, and conductivity ratio [19], while entropy generation remains a key indicator of system irreversibility under conduction, viscous, and magnetic effects [20]. Surface undulations, sinusoidal heating, and wall topologies further alter flow and thermal fields, improving both heat transfer and entropy-based metrics [21]-[23].

Studies of hybrid and multi-phase cavities [24] [25], particularly under MHD influence in trapezoidal geometries, are still limited [26]-[28]. Meanwhile, advanced modeling, including Brownian motion and thermophoresis [29], and finite element techniques [30], has improved accuracy. Recent validation confirms that obstacle shape and wall undulation significantly affect convective behavior in nanofluid systems [31] [32].

Despite extensive research, limited studies have concurrently addressed the combined influence of internal obstacle shape, wall corrugation geometry, and cavity inclination under magnetohydrodynamic (MHD) conditions in trapezoidal nanofluid-filled enclosures. These factors are crucial in engineering applications where precise control of thermal behavior is required under complex boundary conditions. Notably, geometric modifications such as internal obstructions and wall undulations alter flow recirculation, thermal stratification, and entropy generation, particularly when coupled with the damping effects of an external magnetic field.

To fill this research gap, the present study numerically investigates MHD natural convection in a trapezoidal cavity filled with Cu-H_2O nanofluid, incorporating variations in obstacle shapes (square, triangular, and star), wall corrugation profiles (triangular, square, sinusoidal), and inclination angles (15˚, 30˚, 45˚). The Galerkin finite element method is employed to solve the coupled fluid-thermal equations. The study systematically evaluates heat transfer via the Nusselt number (Nu), entropy generation (S_T), and entropy generation-based cooling performance (ECOP). Through comprehensive parametric analysis, the findings aim to identify thermally optimized configurations for advanced passive cooling systems influenced by magnetic and geometric effects.

2. Materials and Methods

This study investigates natural convection and entropy generation within a two-dimensional trapezoidal enclosure filled with Cu-H_2O nanofluid. The cavity features a base angle $\gamma = 15^{\circ}$ and is inclined at $\lambda = 15^{\circ}$, 30˚, and 45˚, to evaluate gravitational reorientation effects. Two uniformly heated solid blocks configured as a star, a square, or a triangle are centrally embedded in the cavity. The top boundary is modeled with sinusoidal, square, or triangular corrugations to examine surface geometry effects. **Figure 1-Figure 3** illustrate these geometric configurations.

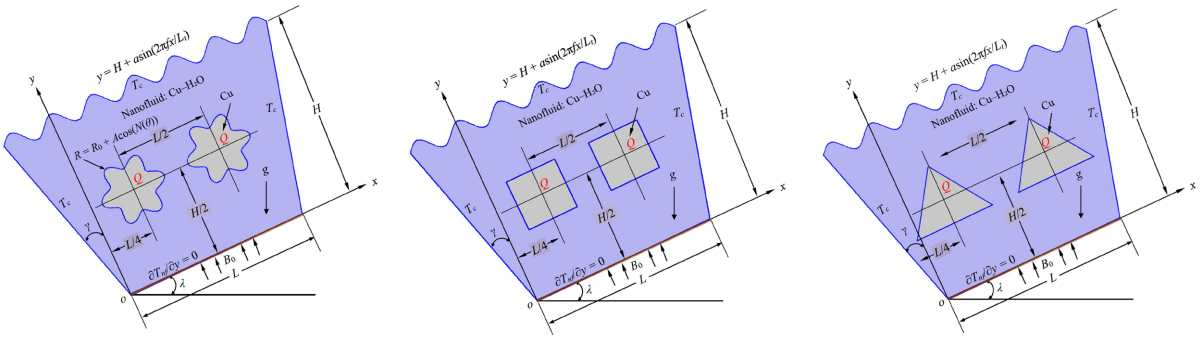

Figure 1. Different geometry with sinusoidal corrugation.

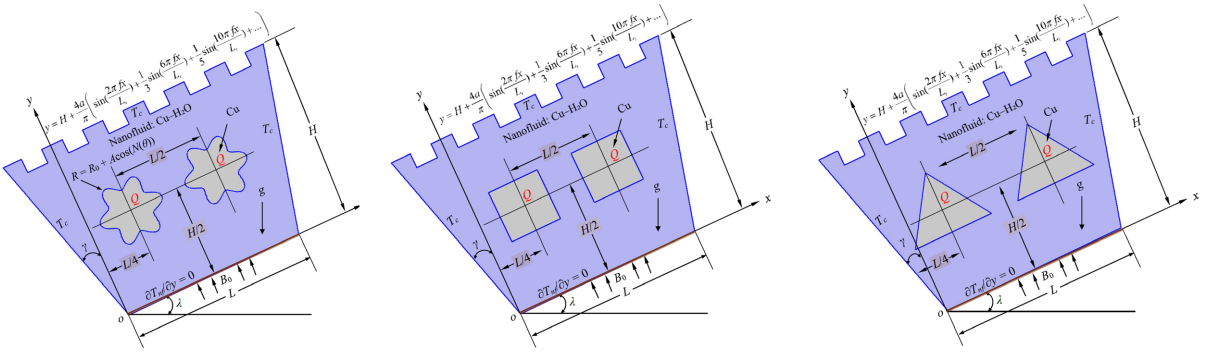

Figure 2. Different geometry with square corrugation.

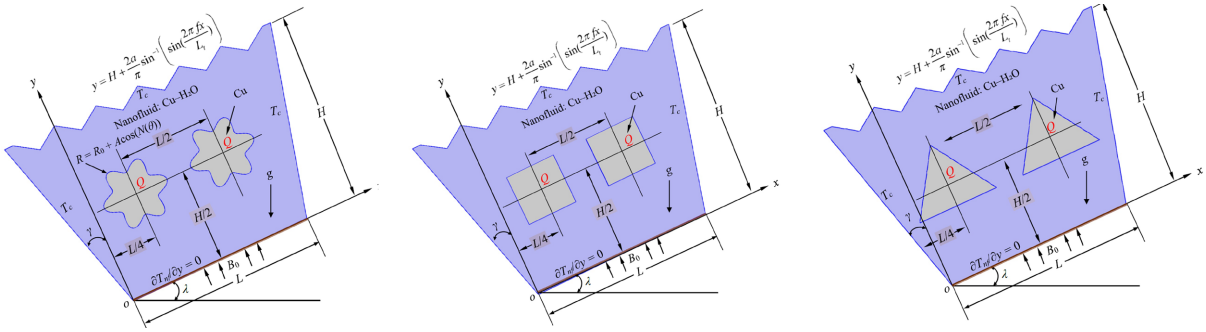

Figure 3. Different geometry with triangular corrugation.

A uniform horizontal magnetic field is applied to account for magnetohydrodynamic (MHD) effects. The top and side walls are maintained at a constant cold temperature, while the inclined bottom wall is adiabatic. All cavity walls and embedded solid surfaces satisfy the no-slip condition. The internal obstacles act as uniform volumetric heat sources. The governing mathematical equations and their non-dimensional forms, which account for natural convection, MHD effects, and nanofluid behavior, boundary conditions are detailed in below [5] [17] [31] [32]:

For Sinusoidal wavy top wall:

$$y = H + a\sin\left(\frac{2\pi fx}{L_t}\right) \tag{1}$$

For Square wavy top wall:

$$y = H + \frac{4a}{\pi}\left(\sin\left(\frac{2\pi fx}{L_t}\right) + \frac{1}{3}\sin\left(\frac{6\pi fx}{L_t}\right) + \frac{1}{5}\sin\left(\frac{10\pi fx}{L_t}\right) + \cdots\right) \tag{2}$$

For Triangular wavy top wall:

$$y = H + \frac{2a}{\pi}\sin^{-1}\left(\sin\left(\frac{2\pi fx}{L_t}\right)\right) \tag{3}$$

Here, H : Height of the cavity, a : Amplitude of the wave, f : Frequency (number of waves), L_t : Total length of the top wall, and x is the position along the wall.

Gravitational acceleration g acts vertically downward, but is decomposed into components along the inclined axis:

$$g_x = g\sin(\lambda),\ g_y = -g\cos(\lambda) \tag{4}$$

Fluid domain:

$$\frac{\partial u}{\partial x} + \frac{\partial v}{\partial y} = 0 \tag{5}$$

$$\rho_{nf}\left(u\frac{\partial u}{\partial x} + v\frac{\partial u}{\partial y}\right) = -\frac{\partial p}{\partial x} + \mu_{nf}\left(\frac{\partial^2 u}{\partial x^2} + \frac{\partial^2 u}{\partial y^2}\right) + \rho_{nf} g\beta_{nf}\left(T_{nf} - T_c\right)\sin(\lambda) - \sigma_{nf}B_0^2 u \tag{6}$$

$$\rho_{nf}\left(u\frac{\partial v}{\partial x} + v\frac{\partial v}{\partial y}\right) = -\frac{\partial p}{\partial y} + \mu_{nf}\left(\frac{\partial^2 v}{\partial x^2} + \frac{\partial^2 v}{\partial y^2}\right) + \rho_{nf} g\beta_{nf}\left(T_{nf} - T_c\right)\cos(\lambda) \tag{7}$$

$$\rho_{nf}C_{p,nf}\left(u\frac{\partial T_{nf}}{\partial x} + v\frac{\partial T_{nf}}{\partial y}\right) = k_{nf}\left(\frac{\partial^2 T_{nf}}{\partial x^2} + \frac{\partial^2 T_{nf}}{\partial y^2}\right) \tag{8}$$

Star-shaped solid domains:

$$k_s\left(\frac{\partial^2 T_s}{\partial x^2} + \frac{\partial^2 T_s}{\partial y^2}\right) + Q = 0 \tag{9}$$

Here, u and v denote velocity components in the x- and y-directions, respectively, and p and T represent pressure and temperature, respectively. The fluid properties are mass density (ρ), thermal conductivity (k), specific heat at constant pressure (C_p), volumetric thermal expansion coefficient (β), and electrical conductivity (σ).

Dimensional Boundary Conditions:

Top Wall:

$$u = v = 0,\ T = T_c \tag{10}$$

Inclined Side Wall:

$$u = v = 0,\ T = T_c \tag{11}$$

Bottom Wall:

$$u = v = 0,\ \frac{\partial T}{\partial x} = 0 \tag{12}$$

Heated Block:

Internal volumetric heat generation applied in the solid domain, Q > 0; conti-

nuity of temperature and heat flux at fluid-solid interfaces is enforced:

$$T_{Fluid} = T_{Solid}, \quad k_{nf} \frac{\partial T}{\partial n_{Fluid}} = k_s \frac{\partial T}{\partial n_{Solid}} \tag{13}$$

$$\rho_{nf} = (1-\phi)\rho_f + \phi\rho_s \tag{14}$$

$$(\rho c_p)_{nf} = (1-\phi)(\rho c_p)_f + \phi(\rho c_p)_s \tag{15}$$

$$\mu_{nf} = \frac{\mu_f}{(1-\phi)^{2.5}} \tag{16}$$

$$k_{nf} = k_f \left[\frac{k_s + 2k_f - 2\phi(k_f - k_s)}{k_s + 2k_f + \phi(k_f - k_s)} \right] \tag{17}$$

$$\beta_{nf} = \left[\frac{(1-\phi)\rho_f \beta_f + \phi\rho_s \beta_s}{\rho_{nf}} \right] \tag{18}$$

Entropy production reflects energy loss from irreversible effects like heat transfer, friction, and MHD forces. In buoyancy-driven MHD flow, entropy is generated through heat transfer, viscous dissipation, and magnetic fields. The local entropy generation due to heat transfer (S_{ht}) in solid and fluid domains is given by:

$$S_{ht} = \frac{k_s}{T_s^2}\left[\left(\frac{\partial T_s}{\partial x}\right)^2 + \left(\frac{\partial T_s}{\partial y}\right)^2\right] + \frac{k_{nf}}{T_{nf}^2}\left[\left(\frac{\partial T_{nf}}{\partial x}\right)^2 + \left(\frac{\partial T_{nf}}{\partial y}\right)^2\right] + \frac{Q_{gen}}{T_s} \tag{19}$$

The local volumetric entropy production due to viscous flow dissipation (S_{ff}) and external magnetic effects (S_{mf}) can be described using the following formulas [5] [17] [31] [32]:

$$S_{ff} = \frac{\mu_{nf}}{T_{nf}}\left[2\left(\frac{\partial u}{\partial x}\right)^2 + 2\left(\frac{\partial v}{\partial y}\right)^2 + \left(\frac{\partial u}{\partial y} + \frac{\partial v}{\partial x}\right)^2\right] \tag{20}$$

$$S_{mf} = \beta_0^2 \frac{\sigma_{nf}}{T_{nf}} v^2 \tag{21}$$

To get the non-dimensional governing equations, the following scales are used:

$$X = \frac{x}{L}, Y = \frac{y}{L}, U = \frac{uL}{\alpha_f}, V = \frac{vL}{\alpha_f}, \theta = \frac{T - T_c}{T_h - T_c}, P = \frac{pL^2}{\mu_{nf}}, Here, \alpha_f = \frac{k_f}{\rho_f c_{p,f}} \tag{22}$$

$$Ra = \frac{g\beta_{nf}(T_h - T_c)L^3}{\nu_{nf}\alpha_f}, \Pr = \frac{\nu_f}{\alpha_f}, Ha = \beta_0 L\sqrt{\frac{\sigma_{nf}}{\mu_{nf}}}, Q^* = \frac{QL^2}{k_{nf}(T_h - T_c)} \tag{23}$$

$$\frac{\partial U}{\partial X} + \frac{\partial V}{\partial Y} = 0 \tag{24}$$

$$\left(U\frac{\partial U}{\partial X} + V\frac{\partial U}{\partial Y}\right) = -\frac{\partial P}{\partial X} + \frac{\mu_{nf}}{\mu_f}\left(\frac{\partial^2 U}{\partial X^2} + \frac{\partial^2 U}{\partial Y^2}\right) + Ra\,\Pr\frac{\rho_{nf}\beta_{nf}}{\rho_f\beta_f}\theta\sin(\lambda) - Ha^2 U \tag{25}$$

$$\left(U\frac{\partial V}{\partial X} + V\frac{\partial V}{\partial Y}\right) = -\frac{\partial P}{\partial X} + \frac{\mu_{nf}}{\mu_f}\left(\frac{\partial^2 V}{\partial X^2} + \frac{\partial^2 V}{\partial Y^2}\right) + Ra\,\Pr\frac{\rho_{nf}\beta_{nf}}{\rho_f\beta_f}\theta\cos(\lambda) \tag{26}$$

$$\left(U\frac{\partial\theta}{\partial X}+V\frac{\partial\theta}{\partial Y}\right)=\frac{k_{nf}}{k_f}\frac{1}{\mathrm{Pr}}\left(\frac{\partial^2\theta}{\partial X^2}+\frac{\partial^2\theta}{\partial Y^2}\right) \tag{27}$$

$$\frac{k_s}{k_{nf}}\left(\frac{\partial^2\theta_s}{\partial X^2}+\frac{\partial^2\theta_s}{\partial Y^2}\right)+Q^*=0 \tag{28}$$

Non-Dimensional Boundary Conditions:

Top Wall:

$$U=V=0,\ \ T=T_c \tag{29}$$

Inclined Side Wall:

$$U=V=0,\ \ T=T_c \tag{30}$$

Bottom Wall:

$$U=V=0,\ \ \frac{\partial T}{\partial X}=0 \tag{31}$$

Heated Block:

Internal volumetric heat generation applied in the solid domain, Q > 0; continuity of temperature and heat flux at fluid-solid interfaces are enforced:

$$T_{Fluid}=T_{Solid},\ \ k_{nf}\frac{\partial T}{\partial N_{Fluid}}=k_s\frac{\partial T}{\partial N_{Solid}} \tag{32}$$

Non-Dimensional Nanofluid Properties:

$$\frac{\rho_{nf}}{\rho_f}=(1-\phi)+\phi\frac{\rho_s}{\rho_f} \tag{33}$$

$$\frac{(\rho c_p)_{nf}}{(\rho c_p)_f}=(1-\phi)+\phi\frac{(\rho c_p)_s}{(\rho c_p)_f} \tag{34}$$

$$\frac{\mu_{nf}}{\mu_f}=\frac{1}{(1-\phi)^{2.5}} \tag{35}$$

$$\frac{k_{nf}}{k_f}=\left[\frac{k_s+2k_f-2\phi(k_f-k_s)}{k_s+2k_f+\phi(k_f-k_s)}\right] \tag{36}$$

$$\beta_{nf}\rho_{nf}=(1-\phi)\rho_f\beta_f+\phi\rho_s\beta_s \tag{37}$$

The thermal behavior of the chamber under different operating conditions is assessed by analyzing the Nusselt number (Nu) of the heated strips and the average fluid temperature (Θ_{av}) inside the domain. The definitions of these quantities are as follows:

$$Nu=\frac{L}{L_s}\left[-\int_{L_0/L}^{2L_0/L}\left.\frac{\partial\Theta}{\partial Y}\right|_{Y=0}dX-\int_{3L_0/L}^{4L_0/L}\left.\frac{\partial\Theta}{\partial Y}\right|_{Y=0}dX\right],\Theta_{av}=\frac{1}{A}\int_A\Theta dA, \tag{38}$$

Here, A represents the non-dimensional surface area of the fluid domain, X and Y are the dimensionless Cartesian coordinates, U and V indicate dimensionless velocity components, and P and Θ are the non-dimensional pressure and temperature of the nanofluid, respectively.

The total entropy generation, expressed as a dimensionless quantity, can be obtained using the following expression:

$$S_T = \frac{T_c^2 L^2}{k_f \Delta T^2 A} \int_A \left(S_{ht} + S_{ff} + S_{mf} \right) dA \tag{39}$$

where A represents the surface area of the computational domain.

The Ecological Coefficient of Performance (ECOP) represents the balance between heat transfer enhancement and thermodynamic irreversibility. A higher ECOP indicates more efficient thermal performance, where greater heat transfer occurs with lower entropy generation. In essence, it quantifies the trade-off between energy utilization and system losses, reflecting the overall thermodynamic sustainability of the convective process. It can be defined as follows to provide a relative estimate of total entropy production associated with heat transfer:

$$ECOP = \frac{S_T}{Nu} \tag{40}$$

The working fluid is a Cu-H_2O nanofluid with a fixed nanoparticle volume fraction of $\varphi = 0.02$, selected for its superior thermal conductivity and MHD compatibility. The simulations cover a Rayleigh number (Ra) range of 10^3 - 10^6 and a Hartmann number (Ha) range of 0 - 50. Thermophysical properties of the nanofluid components, including density, thermal conductivity, specific heat, viscosity, and electrical conductivity, are listed in Table 1 at a reference temperature of 300 K. These properties are essential for modeling buoyancy-driven convection, MHD behavior, and entropy generation.

The Galerkin Finite Element Method (FEM) is used to solve the governing conservation equations for mass, momentum, and energy. Performance is evaluated using the Nusselt number (Nu), Entropy generation (S_T), and Ecological Coefficient of Performance (ECOP).

Table 1. Thermo-physical properties of Water and Cu at $T_m = 300$ K [5] [17] [31] [32].

Name of Property	Symbol	Unit	Water	Cu
Mass Density	ρ	kgm^{-3}	996.6	8933
Specific Heat at Constant Pressure	C_p	$Jkg^{-1}K^{-1}$	4179.2	385
Thermal Conductivity	k	$Wm^{-1}K^{-1}$	0.6102	401
Volumetric Thermal Expansion Coefficient	β	K^{-1}	26.6×10^{-5}	49.9×10^{-6}
Electrical Conductivity	σ	Sm^{-1}	0.05	59.6×10^{-6}
Dynamic viscosity	μ	$kgm^{-1}s^{-1}$	8.538×10^{-4}	-
Prandtl Number	Pr	-	5.856	-

3. Results

This section presents the numerical results for natural convection heat transfer in

a nanofluid-filled trapezoidal cavity under magnetohydrodynamic (MHD) effects. It is divided into two key analyses: Firstly, it examines the influence of different obstacle shapes (square, star, triangular) and wall corrugation types (sinusoidal, square, triangular) on thermal performance; and secondly, it evaluates the impact of varying wall inclination angles (15˚, 30˚, 45˚). The outcomes are discussed in terms of Nusselt number (Nu), entropy generation (S_T), and energy performance (ECOP) across a range of Rayleigh and Hartmann numbers to identify optimal configurations for enhanced heat transfer.

3.1. Obstacle Shapes and Wall Corrugation Effects

The influence of obstacle geometry and wall corrugation on natural convection heat transfer in a nanofluid-filled trapezoidal cavity under magnetic fields is distinctly evident across Table 2-Table 10. For a fixed inclination angle of 15˚, 30˚, and 45˚, and over a range of Hartmann (Ha) and Rayleigh (Ra) numbers, the triangular corrugated wall consistently exhibits superior thermal performance. Particularly, in all inclination cases, the square-shaped obstacles in combination with triangular wavy walls yield the highest Nusselt numbers (Nu), indicating enhanced convective heat transfer. For instance, at $\lambda = 45^{\circ}$ and $Ra = 10^6$, the triangular wall with square obstacles achieves Nu = 6.2401 at Ha = 0 (Table 10), outperforming sinusoidal and square corrugations for the same Ra and obstacle shape (Nu = 6.4137 and 6.2401, respectively).

Table 2. Nu for star-shaped obstacles with different wavy walls at $\lambda = 15^{\circ}$.

Wavy Wall	Ra	Ha = 0	Ha = 15	Ha = 30	Ha = 50
Sinusoidal	10^3	0.79369	0.79369	0.79369	0.79369
	10^4	2.5581	2.5556	2.5533	2.5524
	10^5	3.7556	3.6201	3.4447	3.3369
	10^6	5.7976	5.6067	5.22	4.7166
Square	10^3	0.8018	0.80179	0.80179	0.80179
	10^4	2.6423	2.6404	2.6388	2.6381
	10^5	3.7957	3.6868	3.546	3.4642
	10^6	5.7179	5.5281	5.1568	4.6751
Triangular	10^3	0.79861	0.79861	0.79861	0.79861
	10^4	2.6093	2.6072	2.6054	2.6046
	10^5	3.7736	3.657	3.5047	3.4136
	10^6	5.747	5.5586	5.184	4.6923

Table 3. Nu for square-shaped obstacles with different wavy walls at $\lambda = 15^{\circ}$.

Wavy Wall	Ra	Ha = 0	Ha = 15	Ha = 30	Ha = 50
Sinusoidal	10^3	0.84326	0.84326	0.84325	0.84324

Continued

	10^4	2.6913	2.6881	2.6853	2.684
	10^5	3.9788	3.8277	3.6309	3.5065
	10^6	6.2373	6.0384	5.6553	5.1434
Square	10^3	0.85297	0.85296	0.85295	0.85295
	10^4	2.7849	2.7824	2.7801	2.7792
	10^5	4.0265	3.9039	3.7424	3.6451
	10^6	6.1573	5.9757	5.6151	5.1105
Triangular	10^3	0.84944	0.84943	0.84942	0.84941
	10^4	2.7491	2.7464	2.744	2.7429
	10^5	4.001	3.8709	3.698	3.5913
	10^6	6.1799	5.9944	5.6292	5.1242

Table 4. Nu for triangular-shaped obstacles with different wavy walls at $\lambda = 15^\circ$.

Wavy Wall	Ra	Ha = 0	Ha = 15	Ha = 30	Ha = 50
Sinusoidal	10^3	0.79176	0.79175	0.79175	0.79174
	10^4	2.9106	2.91	2.9094	2.909
	10^5	4.2103	4.113	4.0332	3.9932
	10^6	6.3746	6.1018	5.6317	5.0893
Square	10^3	0.79783	0.79783	0.79783	0.79783
	10^4	2.9817	2.9813	2.9808	2.9806
	10^5	4.2685	4.2055	4.1485	4.1193
	10^6	6.2743	6.007	5.565	5.0441
Triangular	10^3	0.79608	0.79607	0.79607	0.79607
	10^4	2.9563	2.9558	2.9553	2.955
	10^5	4.2449	4.1709	4.106	4.0729
	10^6	6.3262	6.0564	5.6118	5.073

Table 5. Nu for star-shaped obstacles with different wavy walls at $\lambda = 30^\circ$.

Wavy Wall	Ra	Ha = 0	Ha = 15	Ha = 30	Ha = 50
Sinusoidal	10^3	0.79369	0.79369	0.79369	0.79369
	10^4	2.5573	2.555	2.5531	2.5523
	10^5	3.7274	3.5914	3.4249	3.3284
	10^6	5.916	5.5713	5.1574	4.6587
Square	10^3	0.80179	0.80179	0.80179	0.80179
	10^4	2.6417	2.64	2.6386	2.6381
	10^5	3.768	3.6621	3.5307	3.4579
	10^6	5.7008	5.4812	5.1053	4.6249

Continued

Triangular	10^3	0.79861	0.79861	0.79861	0.79861
	10^4	2.6086	2.6068	2.6052	2.6046
	10^5	3.746	3.6311	3.4879	3.4066
	10^6	5.7559	5.5104	5.1294	4.6408

Table 6. Nu for square-shaped obstacles with different wavy walls at $\lambda = 30^\circ$.

Wavy Wall	Ra	Ha = 0	Ha = 15	Ha = 30	Ha = 50
Sinusoidal	10^3	0.84326	0.84325	0.84325	0.84324
	10^4	2.6903	2.6874	2.685	2.6839
	10^5	3.9427	3.7923	3.606	3.4952
	10^6	6.3086	5.9994	5.5697	5.0505
Square	10^3	0.85297	0.85296	0.85295	0.85294
	10^4	2.784	2.7818	2.7799	2.7791
	10^5	3.9912	3.8722	3.7221	3.6364
	10^6	6.1538	5.9156	5.5258	5.0209
Triangular	10^3	0.84943	0.84943	0.84942	0.84941
	10^4	2.7482	2.7458	2.7437	2.7428
	10^5	3.9661	3.8382	3.6762	3.5817
	10^6	6.2045	5.9456	5.5448	5.0349

Table 7. Nu for triangular-shaped obstacles with different wavy walls at $\lambda = 30^\circ$.

Wavy Wall	Ra	Ha = 0	Ha = 15	Ha = 30	Ha = 50
Sinusoidal	10^3	0.7917	0.79175	0.79175	0.79174
	10^4	2.9107	2.91	2.9093	2.909
	10^5	4.2444	4.1236	4.0301	3.9908
	10^6	6.4336	6.1422	5.6355	5.062
Square	10^3	0.79783	0.79783	0.79783	0.79783
	10^4	2.9818	2.9812	2.9808	2.9805
	10^5	4.2976	4.2133	4.1464	4.1175
	10^6	6.3298	6.0446	5.5635	5.0332
Triangular	10^3	0.79607	0.79607	0.79607	0.79607
	10^4	2.9564	2.9558	2.9552	2.955
	10^5	4.2761	4.1798	4.1037	4.071
	10^6	6.3849	6.0977	5.6034	5.053

Table 8. Nu for star-shaped obstacles with different wavy walls at $\lambda = 45^{\circ}$.

Wavy Wall	Ra	Ha = 0	Ha = 15	Ha = 30	Ha = 50
Sinusoidal	10^3	0.79369	0.79369	0.79369	0.79369
	10^4	2.5563	2.5543	2.5528	2.5522
	10^5	3.6784	3.5444	3.3946	3.3161
	10^6	6.0049	5.6188	5.0656	4.5454
Square	10^3	0.80179	0.80179	0.80179	0.80179
	10^4	2.6409	2.6395	2.6384	2.638
	10^5	3.7227	3.6226	3.5074	3.4489
	10^6	5.7374	5.4407	5.0079	4.5273
Triangular	10^3	0.79861	0.79861	0.79861	0.79861
	10^4	2.6077	2.6062	2.605	2.6045
	10^5	3.6994	3.5892	3.4623	3.3965
	10^6	5.8366	5.5031	5.0315	4.5368

Table 9. Nu for square-shaped obstacles with different wavy walls at $\lambda = 45^{\circ}$.

Wavy Wall	Ra	Ha = 0	Ha = 15	Ha = 30	Ha = 50
Sinusoidal	10^3	0.84326	0.84325	0.84324	0.84324
	10^4	2.6889	2.6865	2.6845	2.6837
	10^5	3.8847	3.7354	3.5679	3.4789
	10^6	6.5016	6.0543	5.4486	4.8921
Square	10^3	0.85296	0.85296	0.85295	0.85294
	10^4	2.7828	2.781	2.7796	2.779
	10^5	3.9342	3.8219	3.6914	3.6239
	10^6	6.2066	5.8648	5.3835	4.8712
Triangular	10^3	0.84943	0.84942	0.84941	0.84941
	10^4	2.747	2.745	2.7434	2.7427
	10^5	3.9091	3.7858	3.643	3.5679
	10^6	6.3178	5.9356	5.4113	4.8823

Table 10. Nu for triangular-shaped obstacles with different wavy walls at $\lambda = 45^{\circ}$.

Wavy Wall	Ra	Ha = 0	Ha = 15	Ha = 30	Ha = 50
Sinusoidal	10^3	0.79175	0.7917	0.79174	0.79174

Continued

	10^4	2.9108	2.9099	2.9092	2.9089
	10^5	4.2493	4.1235	4.0242	3.9872
	10^6	6.4137	6.0815	5.5577	4.9866
Square	10^3	0.79783	0.79783	0.79783	0.79782
	10^4	2.9818	2.9812	2.9807	2.9805
	10^5	4.3094	4.2155	4.1424	4.115
	10^6	6.2401	5.9625	5.4986	4.9776
Triangular	10^3	0.79607	0.79607	0.79607	0.79607
	10^4	2.9564	2.9557	2.9552	2.9549
	10^5	4.2855	4.1814	4.0991	4.0681
	10^6	6.3038	6.0068	5.5277	4.9866

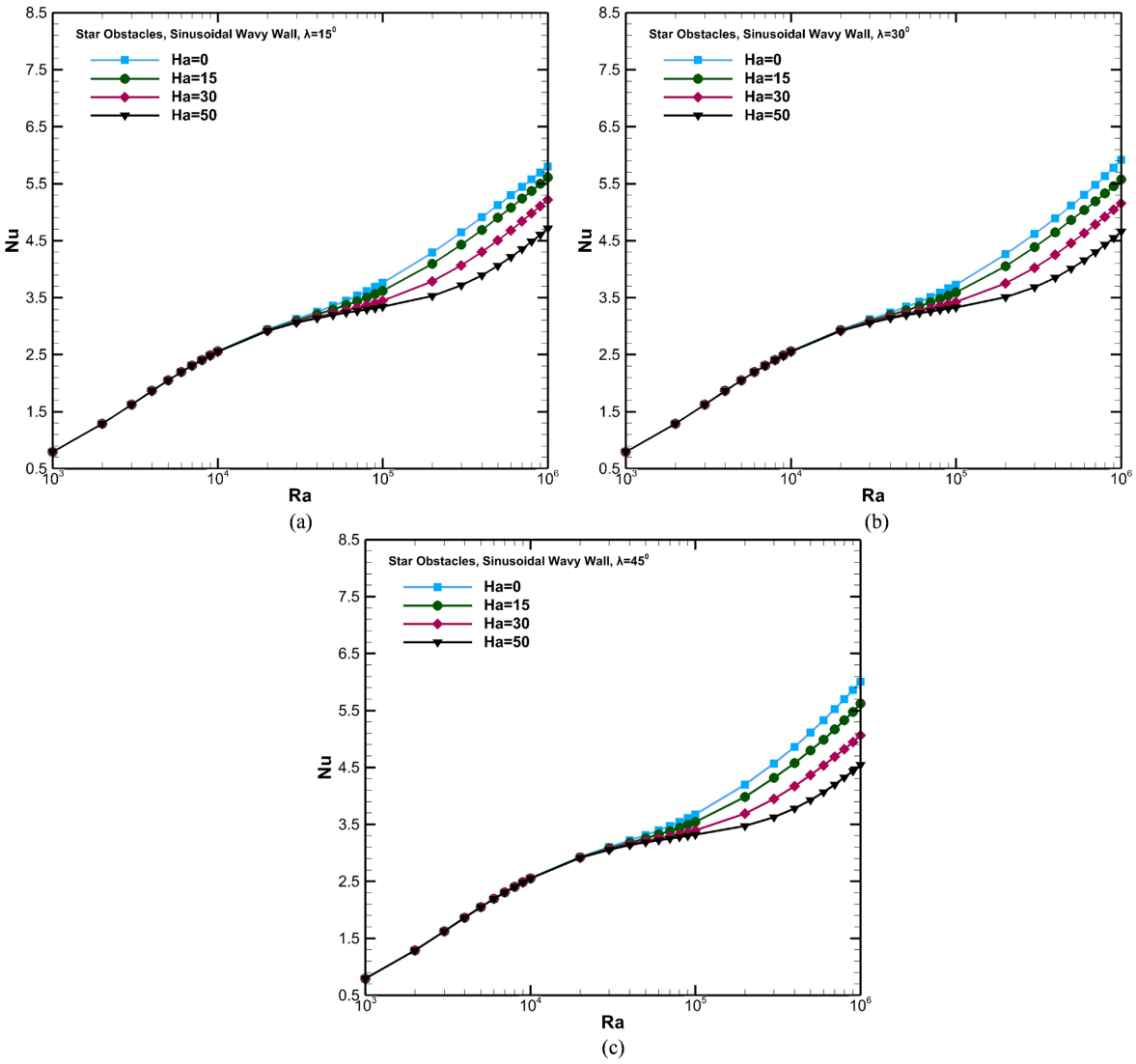

Figure 4. Nu vs Ra for star-shaped obstacles, with sinusoidal wavy wall at (a) $\lambda = 15^\circ$, (b) 30°, (c) 45°.

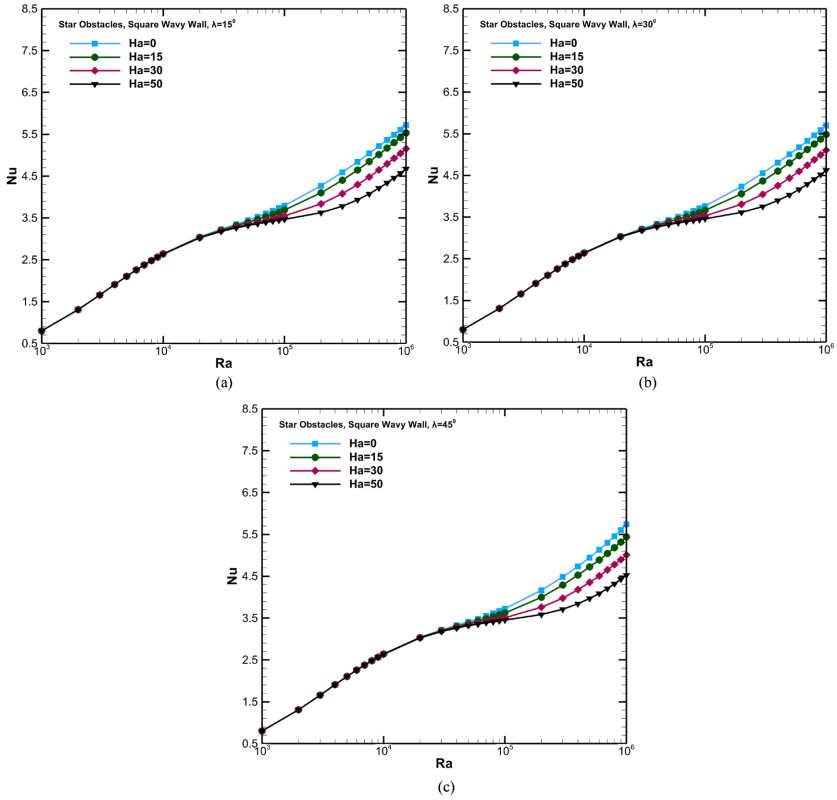

Figure 5. Nu vs Ra for star-shaped obstacles, with square wavy wall at (a) $\lambda = 15^{\circ}$, (b) 30°, (c) 45°.

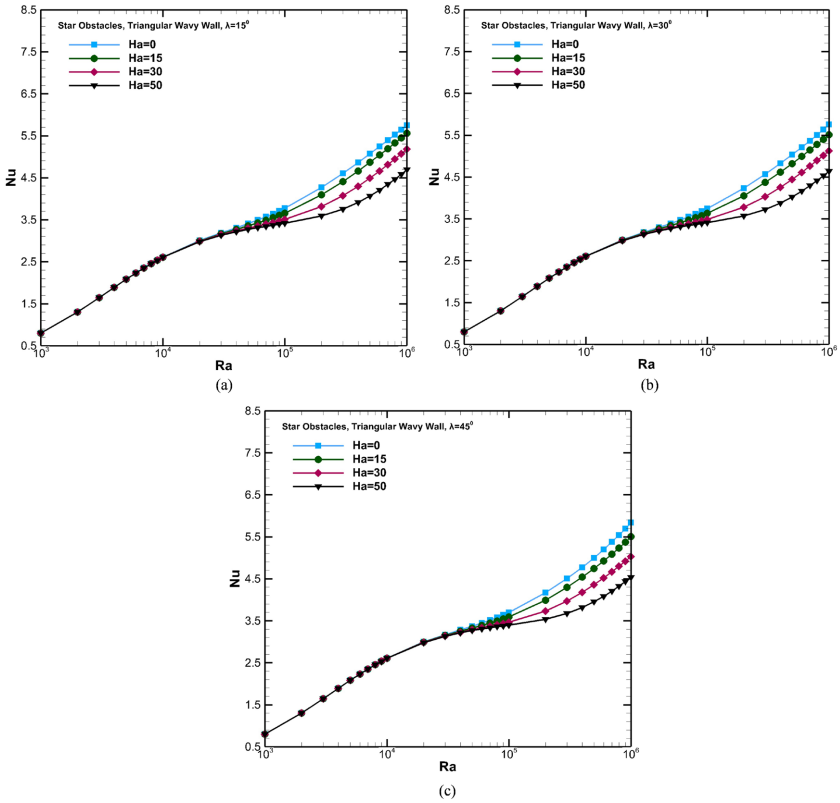

Figure 6. Nu vs Ra for star-shaped obstacles, with triangular wavy wall at (a) $\lambda = 15^{\circ}$, (b) 30°, (c) 45°.

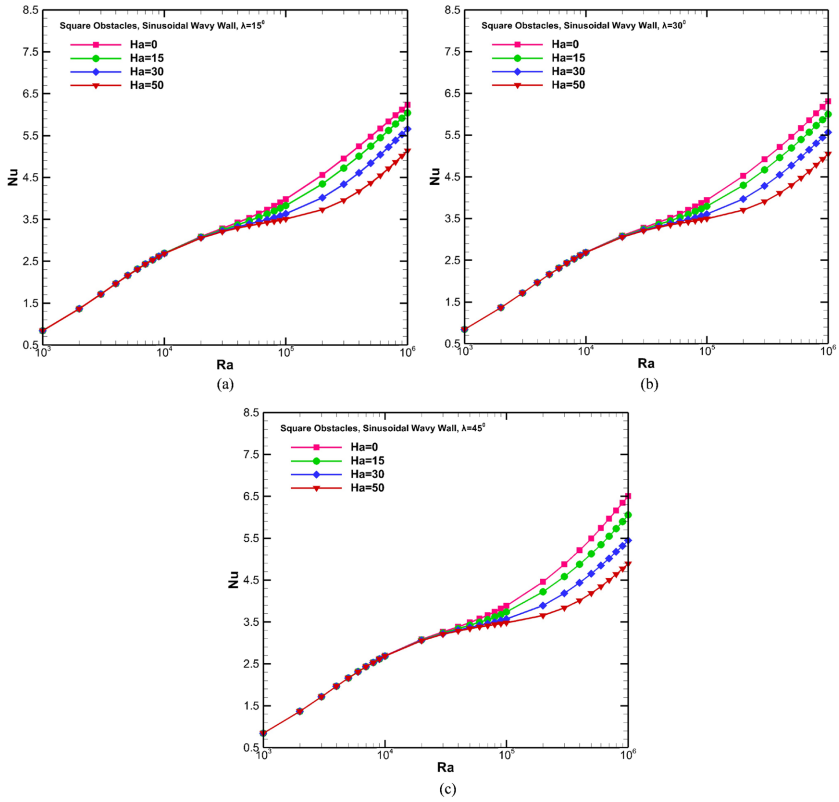

Figure 7. Nu vs Ra for square-shaped obstacles, with sinusoidal wavy wall at (a) $\lambda = 15^{\circ}$, (b) 30°, (c) 45°.

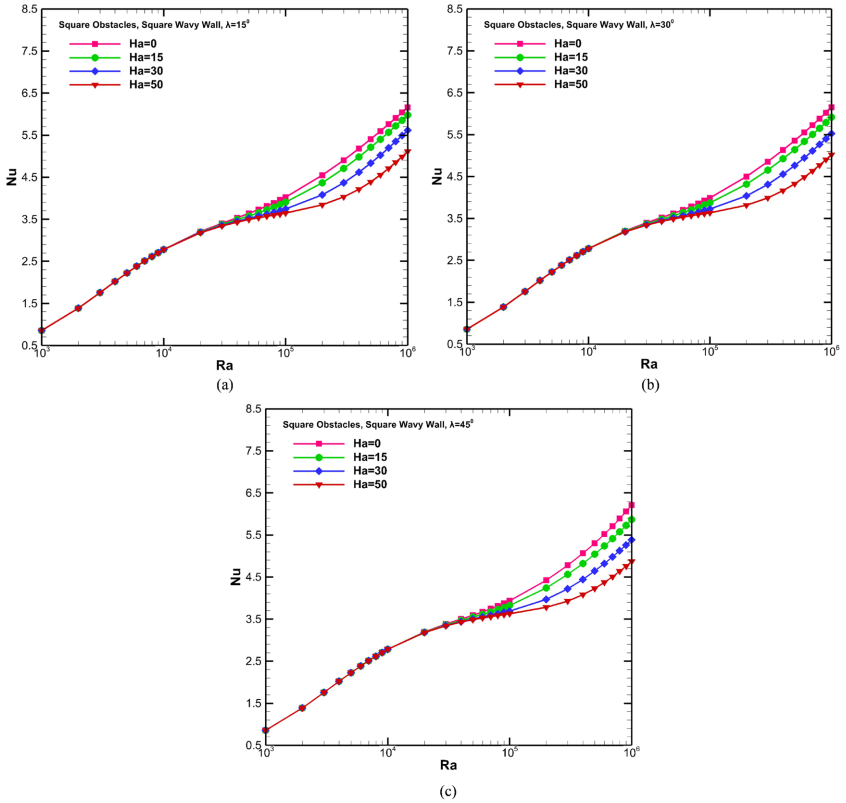

Figure 8. Nu vs Ra for square-shaped obstacles, with square wavy wall at (a) $\lambda = 15^{\circ}$, (b) 30°, (c) 45°.

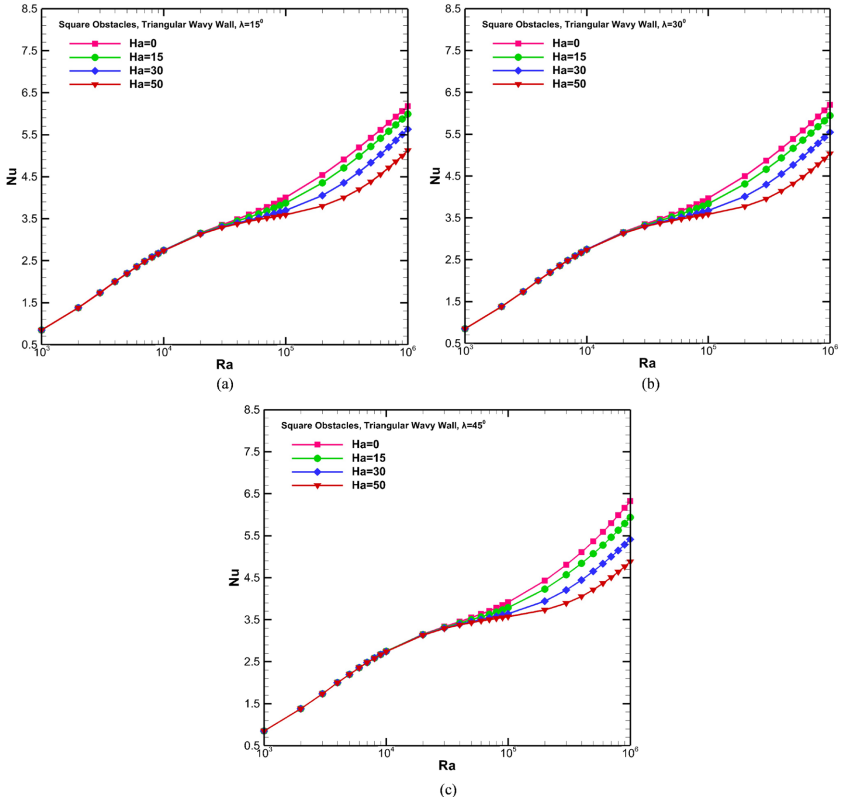

Figure 9. Nu vs Ra for square-shaped obstacles, with triangular wavy wall at (a) $\lambda = 15^{\circ}$, (b) 30°, (c) 45°.

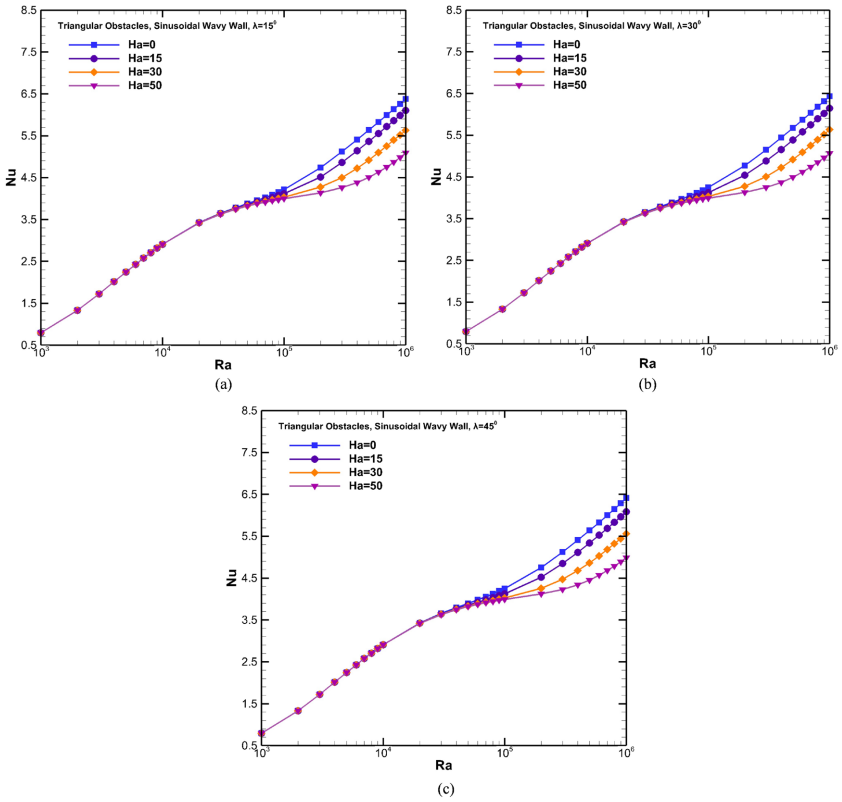

Figure 10. Nu vs Ra for triangular-shaped obstacles, with sinusoidal wavy Wall at (a) $\lambda = 15^{\circ}$, (b) 30°, (c) 45°.

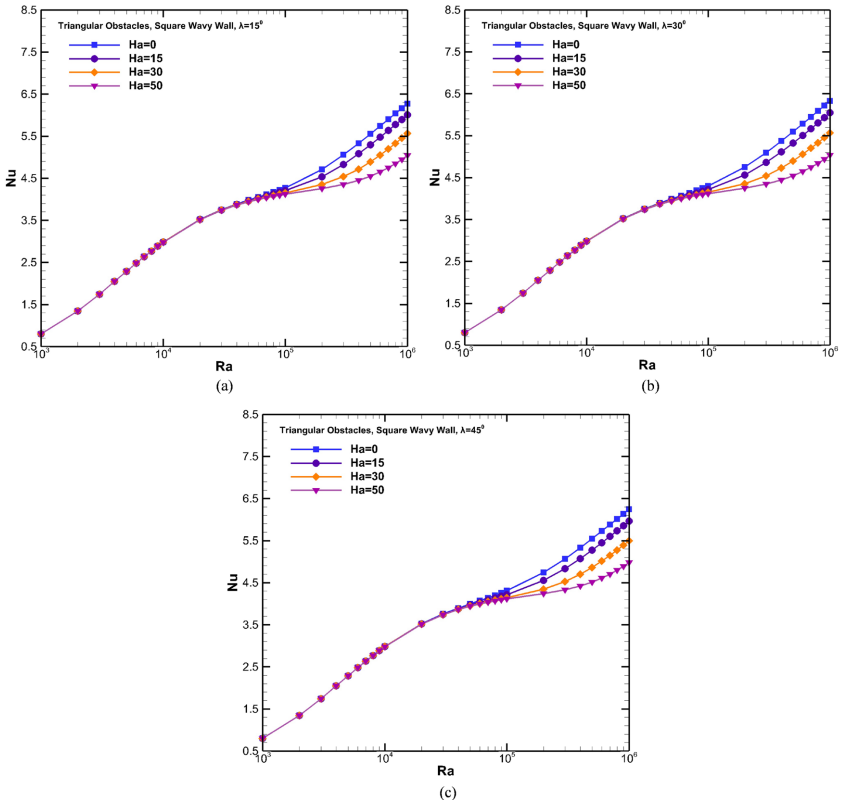

Figure 11. Nu vs Ra for triangular-shaped obstacles, with square wavy wall at (a) $\lambda = 15^{\circ}$, (b) 30°, (c) 45°.

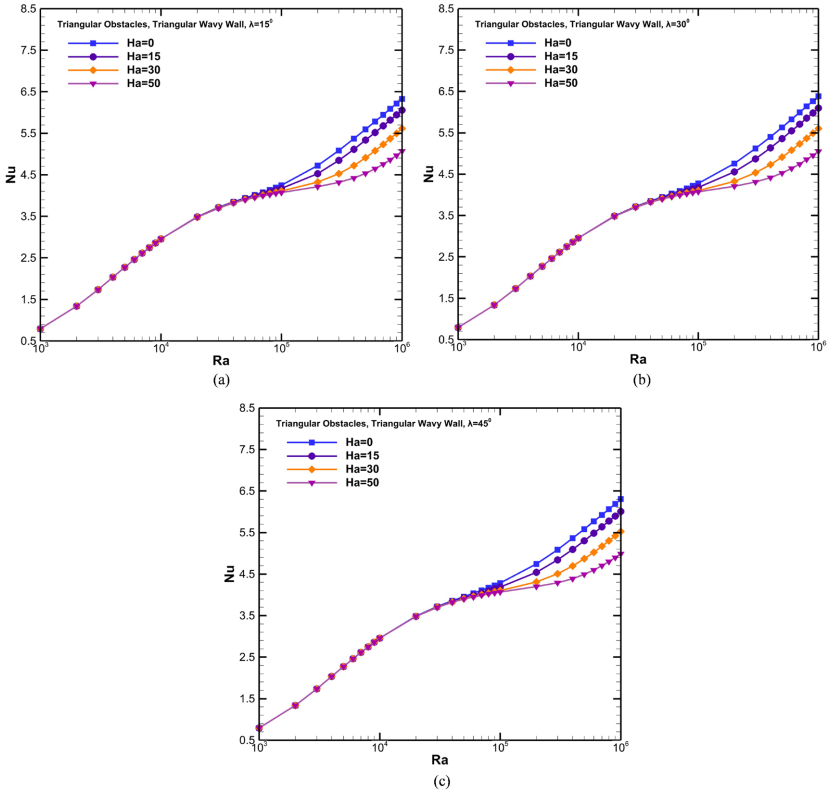

Figure 12. Nu vs Ra for triangular-shaped obstacles, with triangular wavy wall at (a) $\lambda = 15^{\circ}$, (b) 30°, (c) 45°.

Comparatively, across all wall shapes and inclinations, the trend shows that increasing Ha reduces Nu, confirming the suppressive effect of magnetic fields on natural convection. The square wavy walls slightly underperform compared to triangular ones, while sinusoidal walls offer moderate enhancement. As seen in Table 3 and Table 6, square obstacles generally produce higher Nu values than star or triangular shapes, suggesting the role of flow disturbance and vortex formation around angular features in augmenting heat transfer. Overall, the interplay between obstacle shape and wall geometry substantially dictates the convective behavior within MHD-driven nanofluid systems.

Figure 4-Figure 12 illustrate the variation of the Nusselt number (Nu) with Rayleigh number (Ra) for different obstacle shapes (star, square, triangular) and wall corrugation types (sinusoidal, square, triangular) at inclination angles of 15˚, 30°, and 45°, under varying Hartmann numbers (Ha = 0, 15, 30, 50). Across all configurations, Nu increases with Ra, indicating stronger natural convection as thermal buoyancy becomes dominant.

Among the obstacle shapes, square-shaped obstacles consistently yield the highest Nusselt number (Nu), demonstrating superior thermal performance due to strong corner-induced vortex intensification that enhances fluid mixing and heat transfer. Triangular obstacles follow closely, while star-shaped obstacles generally produce lower Nu values under similar conditions.

Regarding wall corrugation, triangular wavy walls promote stronger thermal mixing and circulation zones within the cavity, leading to more vigorous convective motion compared to square or sinusoidal patterns. This enhancement becomes even more pronounced when paired with square or triangular obstacles, as the sharp edges and varying surface gradients jointly intensify local heat transfer and streamline deformation.

Furthermore, the applied magnetic field (Ha) suppresses convective motion across all configurations, leading to a decrease in Nu with higher Ha, illustrating the magnetic damping effect. Nevertheless, cavities featuring square obstacles maintain relatively higher Nu even under stronger magnetic fields, underscoring the significant influence of obstacle geometry and wall corrugation in optimizing thermal performance.

Table 11. S_T for star-shaped obstacles with different wavy walls at $\lambda = 15^{\circ}$.

Wavy Wall	Ra	Ha = 0	Ha = 15	Ha = 30	Ha = 50
Sinusoidal	10^3	16.898	16.898	16.898	16.898
	10^4	0.63853	0.63803	0.63759	0.63742
	10^5	0.021177	0.020913	0.02057	0.02036
	10^6	0.001488	0.001484	0.001476	0.001465
Square	10^3	17.074	17.074	17.074	17.074
	10^4	0.66089	0.66053	0.66021	0.66008
	10^5	0.02199	0.021781	0.02151	0.021354

Continued

	10^6	0.001548	0.001544	0.001536	0.001526
Triangular	10^3	17.014	17.014	17.014	17.014
	10^4	0.65452	0.65412	0.65376	0.65362
	10^5	0.021962	0.021737	0.021442	0.021267
	10^6	0.00156	0.001556	0.001549	0.001539

Table 12. S_T for square-shaped obstacles with different wavy walls at $\lambda = 15^\circ$.

Wavy Wall	Ra	Ha = 0	Ha = 15	Ha = 30	Ha = 50
Sinusoidal	10^3	15.491	15.491	15.491	15.491
	10^4	0.58966	0.58915	0.58871	0.58853
	10^5	0.02063	0.020379	0.020053	0.019848
	10^6	0.001493	0.00149	0.001483	0.001474
Square	10^3	15.659	15.659	15.659	15.659
	10^4	0.61093	0.61055	0.61023	0.6101
	10^5	0.021452	0.021253	0.020993	0.020838
	10^6	0.001555	0.001552	0.001545	0.001537
Triangular	10^3	15.602	15.602	15.602	15.602
	10^4	0.60506	0.60464	0.60428	0.60413
	10^5	0.021427	0.021213	0.020932	0.02076
	10^6	0.001567	0.001564	0.001558	0.00155

Table 13. S_T for triangular-shaped obstacles with different wavy walls at $\lambda = 15^\circ$.

Wavy Wall	Ra	Ha = 0	Ha = 15	Ha = 30	Ha = 50
Sinusoidal	10^3	17.131	17.131	17.131	17.131
	10^4	0.71807	0.71797	0.71788	0.71784
	10^5	0.022264	0.022077	0.021925	0.021849
	10^6	0.001506	0.001502	0.001493	0.001483
Square	10^3	17.243	17.243	17.243	17.243
	10^4	0.7369	0.73683	0.73677	0.73673
	10^5	0.023127	0.023008	0.0229	0.022845
	10^6	0.001569	0.001565	0.001557	0.001547
Triangular	10^3	17.206	17.206	17.206	17.206
	10^4	0.73178	0.7317	0.73163	0.73159
	10^5	0.023083	0.022943	0.02282	0.022758
	10^6	0.00158	0.001576	0.001568	0.001557

Table 14. S_T for star-shaped obstacles with different wavy walls at $\lambda = 30^\circ$.

Wavy Wall	Ra	Ha = 0	Ha = 15	Ha = 30	Ha = 50
Sinusoidal	10^3	16.898	16.898	16.898	16.898
	10^4	0.63838	0.63793	0.63755	0.6374
	10^5	0.021122	0.020857	0.020532	0.020343
	10^6	0.001487	0.001481	0.001473	0.001463
Square	10^3	17.074	17.074	17.074	17.074
	10^4	0.66077	0.66045	0.66018	0.66007
	10^5	0.021937	0.021733	0.021481	0.021342
	10^6	0.001546	0.001541	0.001534	0.001525
Triangular	10^3	17.014	17.014	17.014	17.014
	10^4	0.65439	0.65403	0.65373	0.65361
	10^5	0.021909	0.021687	0.02141	0.021253
	10^6	0.001558	0.001553	0.001546	0.001537

Table 15. S_T for square-shaped obstacles with different wavy walls at $\lambda = 30^\circ$.

Wavy Wall	Ra	Ha = 0	Ha = 15	Ha = 30	Ha = 50
Sinusoidal	10^3	15.491	15.491	15.491	15.491
	10^4	0.58951	0.58905	0.58867	0.58852
	10^5	0.02057	0.02032	0.020012	0.01983
	10^6	0.001492	0.001486	0.00148	0.001472
Square	10^3	15.659	15.659	15.659	15.659
	10^4	0.6108	0.61047	0.6102	0.61009
	10^5	0.021396	0.021202	0.02096	0.020825
	10^6	0.001553	0.001549	0.001543	0.001535
Triangular	10^3	15.602	15.602	15.602	15.602
	10^4	0.60492	0.60455	0.60424	0.60412
	10^5	0.02137	0.021161	0.020897	0.020745
	10^6	0.001565	0.001561	0.001555	0.001548

Table 16. S_T for triangular-shaped obstacles with different wavy walls at $\lambda = 30^\circ$.

Wavy Wall	Ra	Ha = 0	Ha = 15	Ha = 30	Ha = 50
Sinusoidal	10^3	17.131	17.131	17.131	17.131
	10^4	0.7181	0.71797	0.71787	0.71783
	10^5	0.022329	0.022098	0.021919	0.021844
	10^6	0.001506	0.001502	0.001493	0.001481
Square	10^3	17.243	17.243	17.243	17.243
	10^4	0.73692	0.73683	0.73676	0.73673

Continued

	10^5	0.023182	0.023022	0.022896	0.022842
	10^6	0.00157	0.001565	0.001556	0.001546
Triangular	10^3	17.206	17.206	17.206	17.206
	10^4	0.7318	0.7317	0.73162	0.73159
	10^5	0.023143	0.02296	0.022815	0.022754
	10^6	0.001581	0.001576	0.001567	0.001556

Table 17. S_T for star-shaped obstacles with different wavy walls at $\lambda = 45^\circ$.

Wavy Wall	Ra	Ha = 0	Ha = 15	Ha = 30	Ha = 50
Sinusoidal	10^3	16.898	16.898	16.898	16.898
	10^4	0.63818	0.63779	0.6375	0.63739
	10^5	0.021027	0.020765	0.020472	0.020319
	10^6	0.001485	0.001478	0.001469	0.00146
Square	10^3	17.074	17.074	17.074	17.074
	10^4	0.66061	0.66034	0.66014	0.66006
	10^5	0.021851	0.021658	0.021437	0.021325
	10^6	0.001544	0.001538	0.001531	0.001523
Triangular	10^3	17.014	17.014	17.014	17.014
	10^4	0.65422	0.65392	0.65368	0.65359
	10^5	0.02182	0.021606	0.021361	0.021234
	10^6	0.001556	0.00155	0.001542	0.001534

Table 18. S_T for square-shaped obstacles with different wavy walls at $\lambda = 45^\circ$.

Wavy Wall	Ra	Ha = 0	Ha = 15	Ha = 30	Ha = 50
Sinusoidal	10^3	15.491	15.491	15.491	15.491
	10^4	0.5893	0.5889	0.58861	0.5885
	10^5	0.020474	0.020227	0.019949	0.019803
	10^6	0.00149	0.001484	0.001476	0.001468
Square	10^3	15.659	15.659	15.659	15.659
	10^4	0.61063	0.61036	0.61015	0.61008
	10^5	0.021306	0.021122	0.020912	0.020805
	10^6	0.001551	0.001546	0.00154	0.001533
Triangular	10^3	15.602	15.602	15.602	15.602
	10^4	0.60474	0.60443	0.60419	0.60411
	10^5	0.021278	0.021076	0.020844	0.020723
	10^6	0.001564	0.001558	0.001551	0.001544

Table 19. S_T for triangular-shaped obstacles with different wavy walls at $\lambda = 45^\circ$.

Wavy Wall	Ra	Ha = 0	Ha = 15	Ha = 30	Ha = 50
Sinusoidal	10^3	17.131	17.131	17.131	17.131
	10^4	0.71813	0.71796	0.71787	0.71783
	10^5	0.022339	0.022098	0.021907	0.021837
	10^6	0.001505	0.0015	0.00149	0.001479
Square	10^3	17.243	17.243	17.243	17.243
	10^4	0.73693	0.73683	0.73675	0.73673
	10^5	0.023205	0.023027	0.022888	0.022837
	10^6	0.001567	0.001563	0.001554	0.001544
Triangular	10^3	17.206	17.206	17.206	17.206
	10^4	0.73182	0.7317	0.73162	0.73159
	10^5	0.023161	0.022963	0.022807	0.022748
	10^6	0.001578	0.001573	0.001564	0.001553

The effects of obstacle shapes and wall corrugation on the total entropy generation (S_T) were systematically analyzed at varying inclination angles ($\lambda = 15^\circ$, 30°, and 45°), Rayleigh numbers (Ra), and Hartmann numbers (Ha), as presented in Table 11-Table 19. The S_T values consistently decreased with increasing Ra across all configurations, indicating enhanced thermal diffusion dominance over natural convection, which is consistent with prior studies in MHD nanofluid flow regimes.

For all cases, the triangular-shaped wavy walls generally led to slightly higher S_T values at Ra = 10^3 due to increased surface area and flow disturbances enhancing irreversibility. For example, at $\lambda = 15^\circ$, Ra = 10^3, and Ha = 0, the S_T for triangular-shaped obstacles reached 17.206 (Table 13), compared to 17.074 for square and 16.898 for star-shaped ones (Table 11). A similar trend was observed at $\lambda = 30^\circ$ and $\lambda = 45^\circ$ (Table 14 and Table 17), supporting the assertion that triangular geometries induce more vigorous convective behavior.

Regarding wall corrugation, square-shaped wavy walls slightly enhanced entropy generation compared to sinusoidal and triangular types, particularly at lower Ha. For instance, at $\lambda = 30^\circ$, Ra = 10^4, Ha = 0, and square obstacles, S_T = 0.66077 for square walls, while it was lower for sinusoidal (0.63838) and triangular (0.65439) (Table 14). This difference became negligible as Ra increased, with S_T values converging at 10^6 due to MHD dominance.

At higher Ha values (Ha = 50), the influence of both obstacle shape and wall form diminished, with S_T values becoming nearly invariant. For example, across all obstacle shapes and wall types at Ra = 10^3, S_T values remained unchanged as Ha increased from 0 to 50 (Table 11-Table 19), confirming magnetic damping of convection.

In conclusion, triangular-shaped obstacles with square wavy walls promote

maximum entropy generation at low Ra and Ha, while MHD effects suppress these geometric influences at high Ra and Ha, making flow behavior more uniform.

The ECOP values presented in Table 20-Table 28 reveal that obstacle shape, wall corrugation, and inclination angle (λ) significantly influence thermal performance. At low Ra (10^3), ECOP values remain nearly constant across all configurations, indicating conduction-dominated behavior. As Ra increases to 10^6, ECOP rises sharply, especially for square obstacles with sinusoidal walls, which consistently yield the highest ECOP (e.g., 4177.5 in Table 21 at $\lambda = 15^\circ$, Ha = 0).

Table 20. ECOP for star-shaped obstacles with different wavy walls at $\lambda = 15^\circ$.

Wavy Wall	Ra	Ha = 0	Ha = 15	Ha = 30	Ha = 50
Sinusoidal	10^3	0.04697	0.04697	0.04697	0.04697
	10^4	4.0063	4.0054	4.0046	4.0043
	10^5	177.34	173.1	167.46	163.9
	10^6	3896.9	3778	3537.2	3218.6
Square	10^3	0.046959	0.046959	0.046959	0.046959
	10^4	3.9981	3.9974	3.9969	3.9966
	10^5	172.61	169.27	164.85	162.22
	10^6	3694.1	3581.2	3358.1	3063.4
Triangular	10^3	0.046938	0.046938	0.046938	0.046938
	10^4	3.9866	3.9859	3.9852	3.9849
	10^5	171.82	168.24	163.45	160.51
	10^6	3684.9	3572.4	3347.2	3048.4

Table 21. ECOP for square-shaped obstacles with different wavy walls at $\lambda = 15^\circ$.

Wavy Wall	Ra	Ha = 0	Ha = 15	Ha = 30	Ha = 50
Sinusoidal	10^3	0.054436	0.054436	0.054435	0.054435
	10^4	4.5642	4.5627	4.5612	4.5605
	10^5	192.86	187.82	181.07	176.66
	10^6	4177.5	4053.6	3814.3	3488.9
Square	10^3	0.054471	0.054471	0.05447	0.05447
	10^4	4.5584	4.5572	4.5559	4.5553
	10^5	187.7	183.69	178.27	174.92
	10^6	3959.4	3851.2	3634	3325.3
Triangular	10^3	0.054443	0.054442	0.054442	0.054442
	10^4	4.5436	4.5423	4.5409	4.5402
	10^5	186.73	182.47	176.67	172.99
	10^6	3943.8	3832.8	3612.8	3305.8

Table 22. ECOP for triangular-shaped obstacles with different wavy walls at $\lambda = 15^{\circ}$.

Wavy Wall	Ra	Ha = 0	Ha = 15	Ha = 30	Ha = 50
Sinusoidal	10^3	0.046218	0.046218	0.046217	0.046217
	10^4	4.0534	4.0531	4.0527	4.0525
	10^5	189.11	186.3	183.95	182.77
	10^6	4233.7	4063.9	3771	3433
Square	10^3	0.04627	0.04627	0.04627	0.04627
	10^4	4.0463	4.0461	4.0458	4.0456
	10^5	184.57	182.79	181.16	180.31
	10^6	3998.5	3839.2	3575.3	3261
Triangular	10^3	0.046268	0.046268	0.046267	0.046267
	10^4	4.0399	4.0396	4.0393	4.0391
	10^5	183.9	181.79	179.93	178.97
	10^6	4002.9	3843.6	3580.2	3258.8

Table 23. ECOP for star-shaped obstacles with different wavy walls at $\lambda = 30^{\circ}$.

Wavy Wall	Ra	Ha = 0	Ha = 15	Ha = 30	Ha = 50
Sinusoidal	10^3	0.04697	0.04697	0.04697	0.04697
	10^4	4.006	4.0052	4.0045	4.0043
	10^5	176.47	172.19	166.81	163.61
	10^6	3979.7	3762.6	3501.7	3183.8
Square	10^3	0.046959	0.046959	0.046959	0.046959
	10^4	3.9979	3.9973	3.9968	3.9966
	10^5	171.76	168.5	164.36	162.02
	10^6	3688.2	3556.1	3328.2	3033.1
Triangular	10^3	0.046938	0.046938	0.046938	0.046938
	10^4	3.9864	3.9857	3.9851	3.9849
	10^5	170.98	167.44	162.91	160.29
	10^6	3695.3	3547.9	3317.1	3018.6

Table 24. ECOP for square-shaped obstacles with different wavy walls at $\lambda = 30^{\circ}$.

Wavy Wall	Ra	Ha = 0	Ha = 15	Ha = 30	Ha = 50
Sinusoidal	10^3	0.054436	0.054436	0.054435	0.054435
	10^4	4.5637	4.5623	4.5611	4.5604
	10^5	191.67	186.62	180.19	176.26
	10^6	4229	4036.6	3764.6	3431.4
Square	10^3	0.054471	0.05447	0.05447	0.05447
	10^4	4.5579	4.5568	4.5558	4.5552

Continued

	10^5	186.54	182.63	177.58	174.62
	10^6	3962	3818.4	3581.1	3270.5
Triangular	10^3	0.054443	0.054442	0.054442	0.054441
	10^4	4.5431	4.5419	4.5408	4.5401
	10^5	185.59	181.38	175.92	172.65
	10^6	3964.3	3808.9	3565.2	3252.8

Table 25. ECOP for triangular-shaped obstacles with different wavy walls at $\lambda = 30^\circ$.

Wavy Wall	Ra	Ha = 0	Ha = 15	Ha = 30	Ha = 50
Sinusoidal	10^3	0.046218	0.046218	0.046217	0.046217
	10^4	4.0534	4.053	4.0527	4.0524
	10^5	190.08	186.61	183.86	182.69
	10^6	4270.8	4090.6	3775.3	3417.3
Square	10^3	0.04627	0.04627	0.04627	0.04627
	10^4	4.0463	4.046	4.0458	4.0456
	10^5	185.38	183.01	181.1	180.26
	10^6	4032.6	3863	3575.5	3255.4
Triangular	10^3	0.046268	0.046268	0.046267	0.046267
	10^4	4.0399	4.0396	4.0393	4.0391
	10^5	184.77	182.05	179.86	178.91
	10^6	4039.3	3869.9	3576.7	3248.1

Table 26. ECOP for star-shaped obstacles with different wavy walls at $\lambda = 45^\circ$.

Wavy Wall	Ra	Ha = 0	Ha = 15	Ha = 30	Ha = 50
Sinusoidal	10^3	0.04697	0.04697	0.04697	0.04697
	10^4	4.0056	4.0049	4.0044	4.0042
	10^5	174.94	170.69	165.81	163.2
	10^6	4044.6	3801.3	3448.4	3113.6
Square	10^3	0.046959	0.046959	0.046959	0.046959
	10^4	3.9976	3.9971	3.9967	3.9966
	10^5	170.36	167.26	163.61	161.73
	10^6	3716.8	3536.9	3271.5	2973.7
Triangular	10^3	0.046938	0.046938	0.046938	0.046938
	10^4	3.986	3.9855	3.9851	3.9849
	10^5	169.54	166.12	162.09	159.96
	10^6	3750.9	3549.9	3262.3	2957.2

Table 27. ECOP for square-shaped obstacles with different wavy walls at $\lambda = 45^{\circ}$.

Wavy Wall	Ra	Ha = 0	Ha = 15	Ha = 30	Ha = 50
Sinusoidal	10^3	0.054436	0.054435	0.054435	0.054435
	10^4	4.563	4.5618	4.5608	4.5603
	10^5	189.74	184.68	178.85	175.67
	10^6	4362.5	4079.7	3692.5	3332.1
Square	10^3	0.054471	0.05447	0.05447	0.05447
	10^4	4.5573	4.5564	4.5555	4.5551
	10^5	184.66	180.94	176.52	174.18
	10^6	4001.3	3793.3	3497	3178.7
Triangular	10^3	0.054442	0.054442	0.054442	0.054441
	10^4	4.5424	4.5414	4.5405	4.54
	10^5	183.71	179.63	174.78	172.17
	10^6	4040.8	3809.8	3489.1	3161.7

Table 28. ECOP for triangular-shaped obstacles with different wavy walls at $\lambda = 45^{\circ}$.

Wavy Wall	Ra	Ha = 0	Ha = 15	Ha = 30	Ha = 50
Sinusoidal	10^3	0.046218	0.046218	0.046217	0.046217
	10^4	4.0533	4.0529	4.0526	4.0524
	10^5	190.22	186.6	183.69	182.59
	10^6	4260.8	4055.7	3729.7	3372.5
Square	10^3	0.04627	0.04627	0.04627	0.04627
	10^4	4.0462	4.046	4.0458	4.0456
	10^5	185.71	183.07	180.98	180.19
	10^6	3981.2	3815.9	3538	3223.1
Triangular	10^3	0.046268	0.046268	0.046267	0.046267
	10^4	4.0398	4.0395	4.0392	4.0391
	10^5	185.03	182.09	179.73	178.83
	10^6	3995.4	3819.4	3534.2	3210.6

Sinusoidal walls outperform square and triangular ones due to their smoother profiles, enhancing natural convection. Among obstacles, square shapes offer slightly better ECOP than triangular and star-shaped ones. Increasing Ha reduces ECOP across all cases, reflecting magnetic suppression of convection. Additionally, a lower inclination angle ($\lambda = 15^{\circ}$) results in higher ECOP compared to 30˚ or 45˚, emphasizing the thermal advantage of minimal wall tilt. Overall, the optimal configuration for maximizing ECOP is square-shaped obstacles with sinusoidal wavy walls at low Ha and low λ.

3.2. Influence of Inclination Angle

The inclination angle (λ) of wavy walls significantly influences heat transfer behavior, entropy generation, and overall system performance characterized by the Entropy Generation-Based Cooling Performance (ECOP). The present study investigates the impact of three inclination angles 15˚, 30˚, and 45˚ on various obstacle shapes (star, square, and triangular) combined with different wall corrugation patterns (sinusoidal, square, and triangular), over a range of Rayleigh numbers (Ra) from 10^3 to 10^6 and Hartmann numbers (Ha) from 0 to 50.

A key observation is that the Nusselt number (Nu), which indicates convective heat transfer, consistently decreases with increasing inclination. This trend is due to the inclination weakening the buoyancy-driven convection mechanism by displacing the thermal boundary layers and misaligning the temperature gradients with gravity. For instance, square-shaped obstacles with sinusoidal walls at Ra = 10^6 and Ha = 0 exhibited a high Nu of 83.64 at λ = 15˚ (Table 5), which decreased to 77.71 at λ = 45˚ (Table 16). A similar decline is evident for triangular-shaped obstacles with square wavy walls, where Nu dropped from 81.63 at λ = 15˚ (Table 8) to 76.59 at λ = 45˚ (Table 19). This behavior was consistent across all geometries and wall types, confirming that a lower inclination angle fosters stronger thermal convection.

The total entropy generation (S_T) also showed a downward trend with increasing inclination, which is attributed to the reduced convective activity and the subsequent decrease in temperature and velocity gradients. Star-shaped obstacles with triangular wavy walls, for example, showed a notable decrease in S_T from λ = 15˚ (Table 4) to λ = 45˚ (Table 17). Additionally, higher magnetic field strengths (Ha) accelerated this reduction, as the Lorentz force further suppressed convective currents, compounding the effect of inclination. The entropy generation due to heat transfer was more sensitive to these changes than that due to fluid friction, especially at higher Ra.

Among the three parameters analyzed, ECOP was most effective in revealing the thermodynamic performance under varying inclination angles. At λ = 15˚, ECOP values were highest across all obstacle shapes and wall types, signifying the most energy-efficient operation. For triangular obstacles with sinusoidal wavy walls at Ra = 10^6 and Ha = 0, ECOP peaked at 4233.7 (Table 22). However, this value slightly declined to 4260.8 at λ = 30˚ (Table 25) and remained the same at λ = 45˚ (Table 28), highlighting a gradual deterioration in cooling performance. Although this reduction was modest in numerical terms, it indicates a systemic decline in efficiency caused by the misalignment of thermal gradients with the gravitational vector.

Square-shaped obstacles consistently delivered higher ECOP values than their star- and triangular-shaped counterparts. For instance, at Ra = 10^6 and Ha = 0, ECOP for square obstacles with sinusoidal walls was 4177.5 at λ = 15˚ (Table 21), slightly decreasing to 4229 at λ = 30˚ (Table 24) and further to 4362.5 at λ = 45˚

(Table 27). Although ECOP values remained relatively high, the declining trend underscores the impact of inclination on overall system efficiency. For star-shaped obstacles, ECOP rose slightly from 3896.9 (Table 20) at $\lambda = 15^{\circ}$ to 4044.6 (Table 26) at $\lambda = 45^{\circ}$, indicating a minor improvement in thermodynamic performance with increased inclination.

Comparative analysis across the tables further revealed that sinusoidal walls generally yielded the highest ECOP values across all inclination angles, likely due to their smoother transitions that facilitate better fluid motion and heat transfer. Among the obstacle shapes, square-shaped geometries proved to be more resilient to inclination-induced performance drops. Star-shaped obstacles, with their pointed edges and asymmetric geometry, were more susceptible to changes in flow dynamics induced by inclination. For triangular shapes, the performance decline was moderate, positioned between the square and star configurations.

Notably, the combination of low inclination ($\lambda = 15^{\circ}$), high Ra (10^6), and low Ha (0) consistently produced optimal thermal and energy performance across all geometries. For instance, ECOP values at this configuration were 4233.7 for triangular (Table 22), 4177.5 for square (Table 21), and 4044.6 for star obstacles (Table 20), indicating that $\lambda = 15^{\circ}$ is the most thermodynamically favorable orientation. As Ha increased, the damping effect of the magnetic field further compounded the performance loss due to inclination. At higher Ha values, the synergistic suppression of convective motion from both inclination and magnetic forces was especially evident.

In conclusion, increasing the inclination angle from 15˚ to 45˚ consistently reduced the system's thermal and thermodynamic efficiency. This was evidenced by decreasing values of Nu, S_T, and ECOP across all obstacle and wall configurations. The results confirm that maintaining a lower inclination angle is essential for optimizing natural convection-driven systems, especially when coupled with minimal magnetic interference. Among the configurations studied, square-shaped obstacles with sinusoidal walls demonstrated the highest resilience and performance stability under inclined conditions, making them the most suitable choice for applications requiring high energy efficiency and reliable heat transfer in magnetohydrodynamic environments.

4. Discussion

This numerical study examined MHD natural convection in a nanofluid-filled trapezoidal cavity, focusing on the roles of obstacle shape, wall corrugation, and inclination angle. The simulation results were validated against Abdelmalek *et al.* [17], showing strong agreement in thermal profiles and Nusselt number values. As shown in Figure 13, both studies display similar isotherm patterns around star-shaped obstacles at Ra = 10^4, with the present work achieving smoother and more symmetrical contours, likely due to finer grid resolution.

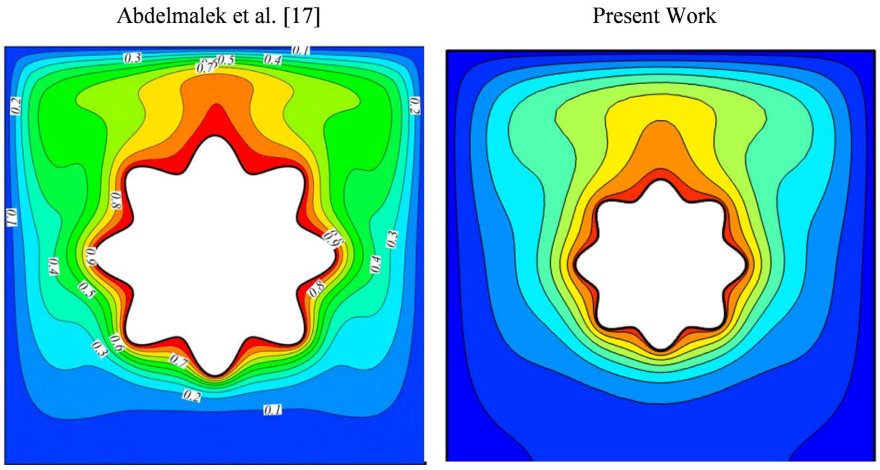

Figure 13. Isotherms for different values of Ra = 10^4 when N = 8, A = 0.15, ϕ = 2%.

Table 29. Comparison of Nu between present work and Abdelmalek *et al.* [17].

Ra	Nanoparticle Volume Fraction (ϕ%)	Present Study	Abdelmalek *et al.* [17]	Deviation (%)
10^3	2	1.1470	1.1307	1.44
10^4	2	2.2944	2.2674	1.19
10^5	2	4.6379	4.5851	1.15
10^6	2	8.9586	8.8341	1.41

Table 29 further supports this validation, with Nusselt number deviations below 1.5% across Ra = 10^3 - 10^6, confirming the accuracy and stability of the current model. These findings underline the impact of geometric complexity and inclination on heat transfer in magnetically influenced nanofluid systems. In particular, the combination of corrugated walls and non-circular obstacles enhances passive thermal control.

The validated model provides a reliable framework for interpreting the thermofluidic behavior of nanofluids under magnetic influence, allowing meaningful insights into practical applications. The results indicate that geometric configuration plays a decisive role in determining whether a system favors maximum heat transfer or optimal thermodynamic efficiency. In engineering practice, systems such as electronic cooling units, high-power microchips, or microchannel heat exchangers prioritize rapid heat dissipation to prevent thermal buildup, thus requiring configurations that yield the highest Nusselt number (Nu). For these purposes, square-shaped obstacles combined with triangular corrugated walls proved most effective, generating strong vortices and high convective flow intensity that enhance local and average heat transfer rates.

In contrast, applications such as solar thermal collectors, heat storage systems, and sustainable energy devices often prioritize maximum Ecological Coefficient of Performance (ECOP), which reflects the trade-off between heat transfer and irreversibility (entropy generation). In such cases, square obstacles with sinusoidal

walls offer the best thermodynamic performance, maintaining efficient energy utilization with minimal entropy production. Hence, while configurations optimizing Nu are ideal for intensive cooling, those maximizing ECOP are more suitable for long-term, energy-efficient thermal management. This distinction highlights how the present model can guide geometry-based optimization of MHD nanofluid systems across a wide range of real-world thermal applications.

5. Conclusions

This numerical investigation explored the effects of obstacle shape, wall corrugation, and inclination angle on magnetohydrodynamic (MHD) natural convection in a nanofluid-filled trapezoidal cavity. The study analyzed heat transfer (Nu), entropy generation (S_T), and thermodynamic efficiency (ECOP) under varying Rayleigh (Ra) and Hartmann (Ha) numbers to identify optimal geometric and operating conditions.

The key findings can be summarized as follows:

1) Heat Transfer: Square-shaped obstacles combined with triangular wavy walls achieved the highest Nusselt numbers, indicating superior convective heat transfer performance.

2) Magnetic Field Effect: Increasing Hartmann number (Ha) reduced Nu and ECOP in all cases, confirming the damping influence of magnetic fields on convective motion.

3) Entropy Generation: Triangular corrugated walls produced slightly higher S_T at low Ra, while magnetic effects minimized geometric influence at high Ha.

4) Energy Efficiency (ECOP): Sinusoidal walls with square obstacles provided the highest ECOP at $\lambda = 15^\circ$ and Ha = 0, showing the most efficient energy conversion.

5) Inclination Angle: Lower inclination angles ($\lambda = 15^\circ$) consistently enhanced heat transfer and efficiency, while higher angles weakened buoyancy effects.

In summary, the optimal configuration for MHD natural convection in nanofluid-filled cavities is achieved with square obstacles, triangular or sinusoidal wavy walls, low inclination (15˚), and minimal magnetic influence. These findings provide practical insights for designing efficient thermal systems in applications such as electronics cooling, solar collectors, and microfluidic devices.

Acknowledgements

The authors gratefully acknowledge the Department of Mathematics, Dhaka University of Engineering and Technology (DUET), Gazipur-1707, Bangladesh, for providing the necessary support and resources to carry out this research work.

Conflicts of Interest

The authors declare no conflicts of interest regarding the publication of this paper.

References

[1] Hidki, R., El Moutaouakil, L., Charqui, Z., Boukendil, M. and Zrikem, Z. (2021) Natural Convection in a Square Cavity Containing Two Heat-Generating Cylinders with Different Geometries. *Materials Today*: *Proceedings*, **45**, 7415-7423. https://doi.org/10.1016/j.matpr.2021.01.626

[2] Cao, Y., Ayed, H., Jarad, F., Togun, H., Alias, H., Issakhov, A., *et al.* (2021) MHD Natural Convection Nanofluid Flow in a Heat Exchanger: Effects of Brownian Motion and Thermophoresis for Nanoparticles Distribution. *Case Studies in Thermal Engineering*, **28**, Article ID: 101394. https://doi.org/10.1016/j.csite.2021.101394

[3] Zheng, J., Zhang, L., Yu, H., Wang, Y. and Zhao, T. (2021) Study on Natural Convection Heat Transfer in a Closed Cavity with Hot and Cold Tubes. *Science Progress*, **104**, 1-25. https://doi.org/10.1177/00368504211020965

[4] Ibrahim, M.N.J., Hammoodi, K.A., Abdulsahib, A.D. and Flayyih, M.A. (2022) Study of Natural Convection Inside Inclined Nanofluid Cavity with Hot Inner Bodies (Circular and Ellipse Cylinders). *International Journal of Heat and Technology*, **40**, 699-705. https://doi.org/10.18280/ijht.400306

[5] Tasnim, S., Mitra, A., Saha, H., Islam, M.Q. and Saha, S. (2023) MHD Conjugate Natural Convection and Entropy Generation of a Nanofluid Filled Square Enclosure with Multiple Heat-Generating Elements in the Presence of Joule Heating. *Results in Engineering*, **17**, Article ID: 100993. https://doi.org/10.1016/j.rineng.2023.100993

[6] Boulahia, Z., Wakif, A. and Sehaqui, R. (2016) Mixed Convection Heat Transfer of Cu-Water Nanofluid in a Lid Driven Square Cavity with Several Heated Triangular Cylinders. *International Journal of Innovation and Applied Studies*, **17**, 82-93.

[7] Ali, A., Ayaz, M., Ahmad, Z. and Marei, A.M. (2025) Analysis of Entropy Generation in Magnetohydrodynamic Convective Flow of Nanofluids within a Wavy Trapezoidal Enclosure: A Brinkmann-Forchheimer Model Using Finite Element Method. *Case Studies in Thermal Engineering*, **73**, Article ID: 106719. https://doi.org/10.1016/j.csite.2025.106719

[8] Nadeem, S., Arif, M., Ullah, I. and Alzabut, J. (2025) MHD Natural Convection of Nanofluid Flow Using a Corrugated Permeable Medium within Corrugated Circular Cavity. *Journal of Thermal Analysis and Calorimetry*, **150**, 5697-5724. https://doi.org/10.1007/s10973-025-14032-y

[9] Dogonchi, A.S., Sadeghi, M.S., Ghodrat, M., Chamkha, A.J., Elmasry, Y. and Alsulami, R. (2021) Natural Convection and Entropy Generation of a Nanoliquid in a Crown Wavy Cavity: Effect of Thermo-Physical Parameters and Cavity Shape. *Case Studies in Thermal Engineering*, **27**, Article ID: 101208. https://doi.org/10.1016/j.csite.2021.101208

[10] Alnajem, M.H.S., Alsabery, A.I. and Hashim, I. (2019) Entropy Generation and Natural Convection in a Wavy-Wall Cavity Filled with a Nanofluid and Containing an Inner Solid Cylinder. *IOP Conference Series*: *Materials Science and Engineering*, **518**, Article ID: 032044. https://doi.org/10.1088/1757-899x/518/3/032044

[11] Chowdhury, K. and Alim, M.A. (2023) Mixed Convection in a Double Lid-Driven Wavy Shaped Cavity Filled with Nanofluid Subject to Magnetic Field and Internal Heat Source. *Journal of Applied Mathematics*, **2023**, Article ID: 7117186. https://doi.org/10.1155/2023/7117186

[12] Boulahia, Z., Wakif, A., Chamkha, A.J., Amanulla, C.H. and Sehaqui, R. (2018) Effects of Wavy Wall Amplitudes on Mixed Convection Heat Transfer in a Ventilated Wavy Cavity Filled by Copper-Water Nanofluid Containing a Central Circular Cold Body. *Journal of Nanofluids*, **8**, 1170-1178. https://doi.org/10.1166/jon.2019.1654

[13] Khatun, S., Kundu, R., Islam, S., Aktary, R. and Kumar, D. (2025) Sensitivity Analysis on Natural Convective Trapezoidal Cavity Containing Hybrid Nanofluid with Magnetic Effect: Numerical and Statistical Approach. *Heliyon*, **11**, e41508. https://doi.org/10.1016/j.heliyon.2024.e41508

[14] Selimefendigil, F. (2017) Natural Convection in a Trapezoidal Cavity with an Inner Conductive Object of Different Shapes and Filled with Nanofluids of Different Nanoparticle Shapes. *Iranian Journal of Science and Technology, Transactions of Mechanical Engineering*, **42**, 169-184. https://doi.org/10.1007/s40997-017-0083-3

[15] Mohammed, A.A., Thaer, M. and Yahya, D.Q. (2022) Mixed Convection Heat Transfer of Al_2O_3-H_2O Nanofluid in a Trapezoidal Lid-Driven Cavity at Different Angles of Inclination. *Texas Journal of Engineering and Technology*, **11**, 20-30.

[16] Mejbel, A., Abdulkadhim, A., Hamzah, R., Hamzah, H. and Ali, F. (2020) Natural Convection Heat Transfer for Adiabatic Circular Cylinder Inside Trapezoidal Enclosure Filled with Nanofluid Superposed Porous-Nanofluid Layer. *FME Transactions*, **48**, 82-89. https://doi.org/10.5937/fmet2001082m

[17] Abdelmalek, Z., Tayebi, T., Dogonchi, A.S., Chamkha, A.J., Ganji, D.D. and Tlili, I. (2020) Role of Various Configurations of a Wavy Circular Heater on Convective Heat Transfer within an Enclosure Filled with Nanofluid. *International Communications in Heat and Mass Transfer*, **113**, Article ID: 104525. https://doi.org/10.1016/j.icheatmasstransfer.2020.104525

[18] Sheikhzadeh, G.A., Nikfar, M. and Fattahi, A. (2012) Numerical Study of Natural Convection and Entropy Generation of Cu-Water Nanofluid around an Obstacle in a Cavity. *Journal of Mechanical Science and Technology*, **26**, 3347-3356. https://doi.org/10.1007/s12206-012-0805-9

[19] Ali, M.M., Alim, M.A., Akhter, R. and Ahmed, S.S. (2017) MHD Natural Convection Flow of CuO/Water Nanofluid in a Differentially Heated Hexagonal Enclosure with a Tilted Square Block. *International Journal of Applied and Computational Mathematics*, **3**, 1047-1069. https://doi.org/10.1007/s40819-017-0400-y

[20] Akram, M., Benhanifia, K., Brahim, M., Rahmani, L., Ansari, A.Z., Eid, M.R., *et al.* (2024) Natural Convection and Flow Patterns of Cu-Water Nanofluids in Hexagonal Cavity: A Novel Thermal Case Study. *Open Physics*, **22**, Article ID: 20240041. https://doi.org/10.1515/phys-2024-0041

[21] Munshi, M.J.H., Bhuiyan, A.H. and Alim, M.A. (2015) A Numerical Study of Natural Convection in a Square Enclosure with Non-Uniformly Heated Bottom Wall and Square Shape Heated Block. *American Journal of Engineering Research* (*AJER*), **4**, 124-137.

[22] Chowdhury, K., Alim, A. and Hossen, M. (2020) Natural Convection in a Partially Heated and Cooled Square Enclosure Containing a Diamond Shaped Heated Block. *International Journal of Fluid Mechanics & Thermal Sciences*, **6**, 1-8. https://doi.org/10.11648/j.ijfmts.20200601.11

[23] Saha, B.K., Jihan, J.I., Barai, G., Moon, N.J., Saha, G. and Saha, S.C. (2025) Exploring Natural Convection and Heat Transfer Dynamics of Al_2O_3-H_2O Nanofluid in a Modified Tooth-Shaped Cavity Configuration. *International Journal of Thermofluids*, **25**, Article ID: 101005. https://doi.org/10.1016/j.ijft.2024.101005

[24] Sompong, P. and Witayangkurn, S. (2013) Natural Convection in a Trapezoidal Enclosure with Wavy Top Surface. *Journal of Applied Mathematics*, **2013**, Article ID: 840632. https://doi.org/10.1155/2013/840632

[25] Suresh Reddy, E. and Panda, S. (2022) Heat Transfer of MHD Natural Convection Casson Nanofluid Flows in a Wavy Trapezoidal Enclosure. *The European Physical*

Journal Special Topics, **231**, 2733-2747.
https://doi.org/10.1140/epjs/s11734-022-00609-3

[26] Alomari, M.A., Al-Farhany, K., Hashem, A.L., Al-Dawody, M.F., Redouane, F. and Olayemi, O.A. (2021) Numerical Study of MHD Natural Convection in Trapezoidal Enclosure Filled with (50%MgO-50%Ag/Water) Hybrid Nanofluid: Heated Sinusoidal from Below. *International Journal of Heat and Technology*, **39**, 1271-1279. https://doi.org/10.18280/ijht.390425

[27] Rahaman, M.M., Bhowmick, S. and Saha, S.C. (2025) Thermal Performance and Entropy Generation of Unsteady Natural Convection in a Trapezoid-Shaped Cavity. *Processes*, **13**, Article 921. https://doi.org/10.3390/pr13030921

[28] Alshayji, A., Alzuabi, M.K. and Aljuwayhel, N.F. (2025) Numerical Investigation of Nanofluid Free Convection in a Rectangular Cavity Using Variable Properties. *Journal of Thermal Analysis and Calorimetry*, **150**, 6519-6538. https://doi.org/10.1007/s10973-025-14197-6

[29] El hadoui, B. and Kaddiri, M. (2025) Optimizing Nanofluid-Enhanced Mixed Convection in Inclined Rectangular Chambers. *Journal of Thermal Analysis and Calorimetry*, **150**, 12717-12733. https://doi.org/10.1007/s10973-025-14491-3

[30] Uddin, M.J., Al Kalbani, K.S., Rahman, M.M., Alam, M.S., Al-Salti, N. and Eltayeb, I.A. (2016) Fundamentals of Nanofluids: Evolution, Applications and New Theory. *International Journal of Biomathematics Systems Biology*, **2**, 1-32.

[31] Ali, M.M., Akhter, R. and Alim, M.A. (2020) MHD Natural Convection and Entropy Generation in a Grooved Enclosure Filled with Nanofluid Using Two-Component Non-Homogeneous Model. *SN Applied Sciences*, **2**, Article No. 571. https://doi.org/10.1007/s42452-020-2319-x

[32] Deep, S.S., Sultana, S., Haque, T., Rahman, M.T. and Saha, S. (2025) Coupled Fluid-Thermal Analysis of a Square Chamber with a Wavy Top Wall and an Internal Solid Elliptical/Circular Block. *Applications in Engineering Science*, **24**, Article ID: 100268. https://doi.org/10.1016/j.apples.2025.100268